Motion-Guided Scar Detection from Static Left Atrial MRI via Deformable Registration to a Healthy Atlas

Bipasha Kundu[a], Richard Simon[b], and Cristian Linte[a,b]

[a]Center for Imaging Science, Rochester Institute of Technology, Rochester, NY 14623, USA
[b]Department of Biomedical Engineering, Rochester Institute of Technology, Rochester, NY

ABSTRACT

Accurate identification and localization of left atrial (LA) scar tissue provides critical information for guiding catheter ablation therapy in atrial fibrillation (Afib). However, the assessment of LA scar from motion remains challenging due to the lack of standardized imaging protocols and motion-resolved data, compounded by the thin atrial wall, variability across patients, and limitations in spatial resolution of MRI. To overcome these limitations, we propose a framework that infers scar regions from static late gadolinium-enhanced (LGE)-MRI by analyzing abnormal motion patterns derived from deformable registration to a healthy motion atlas.

Our method combines 3D segmentation method with deformable registration to a cine derived LA atlas constructed from healthy subjects. While direct scar segmentation from LGE-MRI is often unreliable due to poor contrast and heterogeneity, LA segmentation is highly consistent and reproducible, serving as a robust anatomical prior. The segmented LA masks enable accurate shape-based alignment and facilitate the extraction of deformation vector fields (DVFs). We compute the voxel-wise Mahalanobis distance between the patient DVF magnitude and healthy atlas statistics within a morphologically defined left atrial mask. This helps to quantify deviations from normal motion, and voxels exceeding an adaptive threshold are labeled as regions of abnormal motion. These motion outliers, constrained by the wall, indicate functionally stiff atrial tissue regions that often extend beyond the LGE-defined scar core, serving as biomarkers of diffuse tissue remodeling.

Unlike traditional methods that require full-cycle cine data or motion-resolved contrast sequences, our framework supports scar detection and localization from static LGE-MRI alone. We implemented two 3D segmentation frameworks, nnUNet and nnFormer, and evaluated three deformable registration strategies—SimpleITK-DDVF, ANTs, and BSpline and demonstrated that our approach achieves reliable performance without the need for highly accurate scar segmentation. These results demonstrate that motion-based markers can complement conventional intensity-based methods and and have the potential to improve ablation therapy planning by identifying scarred areas that should be avoided during treatment.

Keywords: Atrial fibrillation, left atrium, scar tissue, ablation therapy, motion, deformable registration

1. INTRODUCTION

The anatomical and functional analysis of the left atrium (LA) and scar are crucial for the diagnosis and treatment planning of atrial fibrillation (Afib).[1] Successful ablation therapy relies on precise localization of arrhythmogenic (mechanically stiff and functionally abnormal), particularly scar tissue in the LA. By analyzing abnormal motion patterns derived from the deformation fields, we can infer the presence of scar tissue in the LA, enabling more precise targeting of ablation zones. However, LA anatomy presents unique challenges for image-guided therapy planning: its thin myocardial wall, complex structural variability, and lack of standardized imaging protocols complicate both scar identification and treatment targeting.[2,3] While late gadolinium enhanced (LGE)-MRI is the clinical gold standard for scar imaging and detection, scar segmentation accuracy remains limited, with Dice scores in the range of $0.55 - 0.64$, as reported in previous studies.[4–6] Importantly, supervised static segmentation

Further author information:
Bipasha Kundu: E-mail: bk7944@g.rit.edu
Richard Simon: E-mail: rasbme@rit.edu
Cristian A. Linte: E-mail: calbme@rit.edu

of scar is limited by inaccurate manual annotations, inter-observer variability, partial volume effects in thin atrial walls, and poor contrast. Furthermore, such approaches cannot capture dynamic abnormalities and motion abnormalities to sufficiently accurately predict arrhythmia risk. Importantly, prior studies have shown that ablation outcome is more strongly associated with the spatial distribution and functional impact of atrial fibrosis than with absolute scar volume.[7] In our registration framework, the LA mask is used for global alignment, whereas the scar error affects the local refinement.

Recent advances in medical image-based modeling suggest that abnormal tissue motion can serve as a biomarker for fibrosis, as scarred regions exhibit altered biomechanics (e.g., reduced contractility or stiffness).[1] The potential for identifying scar tissue from the motion of the LA primarily depends on the full cardiac cycle of the data, which encompasses tissue biomechanics, stiffness, and fibrotic regions. However, most existing methods rely on sparse temporal MRI acquisitions or the availability of full cardiac cycle motion data, as well as annotated LA data with scar regions, which is absent in public Afib datasets.

To address this limitation, we propose an atlas-based framework for image-guided scar identification for Afib therapy planning that bypasses reliance on segmentation by deriving scar presence from biomechanical dysfunction. Our approach uses initial LA segmentation solely as a partial reference to compute motion abnormalities via deformable registration to a healthy motion atlas (built from a set of healthy individuals) and scar detection itself is performed independently using motion-derived statistical abnormalities.

Voxel wise Mahalanobis distances between patient DVF magnitudes and healthy atlas statistics are computed within a morphologically derived atrial wall mask, identifying statistically significant deviations from normal motion (Mahalanobis distance $> \mu + \mathrm{k}\sigma$). These unsupervised motion outliers delineate regions of atrial stiffness that extend beyond discrete LGE scar cores.

Our key contributions are as follows: (1) We introduce a deformation registration-based scar detection pipeline tailored for static LGE-MRI, and (2) we demonstrate that unsupervised motion abnormality estimation using a healthy atlas statistics can reveal scar regions without requiring cine sequences or manual annotations.

2. METHODOLOGY

2.1 Dataset Description

We used two different datasets for our work. The first dataset contains the static frame that incorporates the LA cavity and scar data, and the second dataset is used to create the reference atlas from the healthy populations.

LAScarQS 2022. The LascarQS 2022 (Task 1) dataset[8–10] provides 60 post-ablation LGE 3D cardiac MRI scans with manual segmentation of the LA and atrial scar tissue annotated separately. Each case includes a static-phase LGE image acquired with two different voxel sizes: $576 \times 576 \times 44$ and $640 \times 640 \times 88$ voxels, both with the same voxel dimensions of $0.625 \times 0.625 \times 2.5\ mm^3$.

Aladdin CMR LA Data. We used the healthy subset of the ALADDIN dataset,[11] which includes 3D Cine MRI balanced steady-state free precession (bSSFP) scans of the LA acquired from 10 healthy volunteers (mean age: 30.4 ± 4.7 years; 40% female). Scans were obtained using a 1.5T Philips Ingenia scanner with a 32-channel cardiac coil and a high-resolution ECG-gated protocol. Each volume consists of 36 slices with a spatial resolution of $1.72 \times\times 1.72 \times 2.00\ mm^3$, covering the entire cardiac cycle across 20 phases.

2.2 Proposed Framework

We propose a new framework to analyze left atrial displacements and deformations, as well as motion abnormalities, to identify scar from the static LGE-MRI frame. Fig. 1 shows the overall pipeline for detecting scars.

2.2.1 Segmentation Network

We formulate the segmentation task as a multi-label volumetric segmentation problem targeting both the LA and atrial scar. The proposed scar detection framework itself is independent of the scar segmentation accuracy and relies exclusively on motion-derived abnormalities. We adopted nnUNet v2 (3D)[12] and the transformer-based volumetric segmentation framework nnFormer (3D)[13] as backbone architectures for joint segmentation of the LA cavity and scar tissue. We used 80% of the data for training and the remaining 20% for testing. The remaining

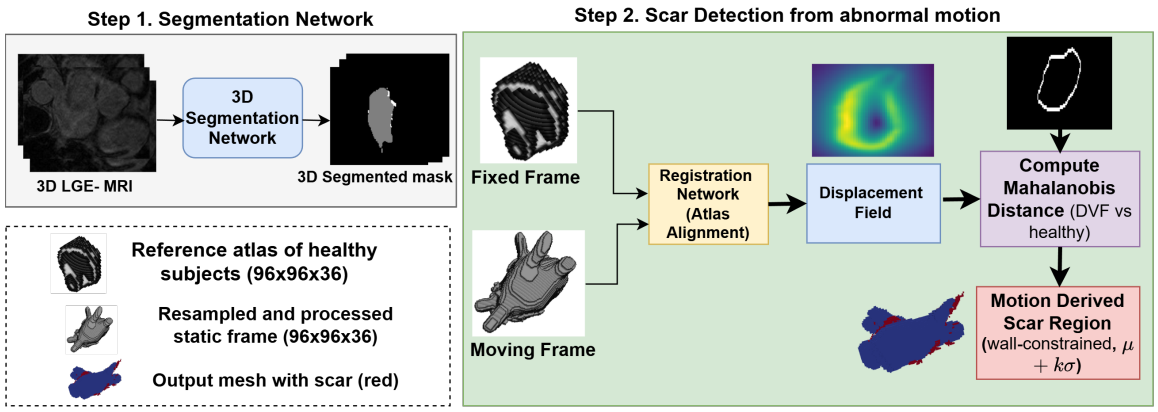

Figure 1. Overview of the proposed scar detection pipeline. A 3D segmentation network extracts the left atrium (LA) mask from static LGE-MRI. The segmented moving frame is deformably registered to a healthy atlas (fixed frame) using a registration network to estimate the displacement field. The Mahalanobis distance is computed over this field to identify abnormal motion. Regions exceeding an adaptive threshold are labeled as scar tissue (red).

20% of the data were subsequently used as input to the registration network. We implemented nnUNet and nnFormer with all its default parameter settings and 1000 epochs. Using nnUNet, we achieved an LA cavity Dice score of 0.91 ± 0.02, and and a scar Dice of 0.49 ± 0.07. In contrast, nnFormer achieved an LA cavity Dice Score of 0.92 ± 0.02 and and a scar Dice of 0.51 ± 0.06. However, as mentioned earlier, segmentation outputs do not directly define or supervise scar detection. To ensure that abnormal motion is evaluated only within meaningful myocardial tissue, an LA wall mask is created by dilating the LA cavity segmentation and excluding the blood pool. Later Mahalanobis based abnormality detection is applied only within this wall region. This limits scar localization to the atrial myocardium and is fully driven by motion statistics.

2.2.2 Pre-Processing

Since the two datasets used for the registration task were acquired from various scanners under different imaging conditions and had differing spatial dimensions, we performed several pre-processing steps to ensure compatibility before applying deformable registration. To ensure consistency in the number of axial slices across the segmentation volumes of both datasets, we applied a standardized Z-axis adjustment procedure. Each volume was adjusted to a fixed depth of 36 slices along the Z-axis to match the atlas of the healthy subset. If a volume had more than 36 slices, central slices were retained by cropping symmetrically from both ends. If it had fewer than 36 slices, zero-padding was applied equally at the top and bottom. This ensured consistent input dimensions across all samples while preserving the anatomical center of the volume.

2.2.3 Spatial Cropping and 3D Volume Reconstruction

To ensure spatial standardization of the segmented structures, we applied centroid-based cropping to each 2D axial slice of the Z-adjusted segmentation masks. Each slice was treated as a grayscale image where all non-zero pixels were considered foreground. We calculated the 2D centroid of the segmented mask of the LA cavity and extracted a 96×96 crop centered at this point. After processing all slices, the cropped 2D slices were stacked to form a 3D multi-label segmentation volume with a uniform voxel spacing of 1.72×1.72×2.0 mm and the same origin and directions, ensuring compatibility with downstream registration and analysis pipelines.

2.3 Atlas Generation

We adopted a registration pipeline analogous to brain atlas creation methods,[14–17] but adapted for cardiac motion analysis. Cardiac phase 0 (end-diastole) from each healthy case was aligned to a randomly selected reference case through a multi-stage approach as mentioned in.[18] The cardiac motion atlas was generated from a cohort of healthy subjects using an affine registration pipeline, using a mean square error (MSE) and gradient descent

optimization to refine the affine registration (global alignment) and diffeomorphic non-rigid registration (local deformations). To avoid randomly selected reference bias and make it patient-specific, we computed the average inverse transform for each case using a similar strategy mentioned in,[14,18] as follows:

$$\overline{T^{-1}} = \frac{1}{n}\sum_{i=1}^{n} T_i^{-1}, \tag{1}$$

where n is the number of cases, and T_i^{-1} is the inverse of the forward transform for the i^{th} case. Finally, DVFs from individual cases were warped to atlas space using the composite transforms, enabling population-wide analysis of cardiac motion patterns.

2.4 Deformable Registration

We used the predicted multilabel segmentation mask from nnUNet and nnFormer to register it with the healthy motion atlas to find the abnormal motion. We used three different deformable registration methods for our experiments. SimpleITK Dense-DVF, ANTs (SyN), and BSpline (FFD) were implemented to calculate the DVFs, which was later used for evaluation.

2.4.1 Mahalanobis Distance for abnormal motion and Scar Detection

Scar detection emerges from motion abnormalities in the DVF when registering a stiff atrial fibrillation LA region to a healthy atlas. Since the Afib scar is locally stiff, registering it to a healthy subset requires a large DVF in those regions, making them Mahalanobis outliers. We computed the voxel-wise Mahalanobis distance between the subject's deformation field magnitude and that of a healthy motion atlas. For each healthy patient, end-diastole frames were registered to the atlas using SimpleITK, and the resulting DVF was extracted. Further, voxel-wise DVF magnitudes were stacked across all healthy subjects to compute the mean (μ_h) and standard deviation (σ_h) at each voxel for Mahalanobis-based abnormality detections. An adaptive threshold ($\mu+k\sigma$) was applied to detect regions exhibiting abnormal motion, where k is a constant that controls how many standard deviations above the mean we consider "abnormal". In this study, k was set to 3. To anatomically constrain detections to the thin atrial myocardium (around 1-3 mm), we derived a wall mask by dilating the warped LA cavity (label 1) by 2 voxels, and the abnormal motion regions were identified within this wall mask only. This conservative adaptive threshold and anatomical constraint ensure detections focus on statistically significant myocardial outliers, enabling robust scar localization despite variable image quality or segmentation performance. Voxels exceeding this threshold were classified as regions featuring abnormal motion. These regions are interpreted as scar tissue and should be avoided during ablation to ensure effective treatment planning. This allowed for the quantification of voxel-wise motion abnormalities relative to healthy variation, enabling the detection of regions that deviated significantly from expected motion patterns. The Mahalanobis distance D_M quantifies how far a voxel's deformation deviates from healthy population statistics following the equation.

$$D_M(x,y,z) = \frac{(M_p(x,y,z) - \mu_h(x,y,z))^2}{\sigma_h^2(x,y,z)}, \tag{2}$$

where M_p is patient DVF magnitude.

3. RESULTS

To assess the quality and anatomical plausibility of the deformation fields generated during registration, we computed the Jacobian determinant of the transformation defined by the estimated DVFs that map the static-frame patient segmentation (containing both LA and scar labels) to the healthy reference atlas, following equation.

$$\det(J_\phi(\mathbf{x})) = \left|\frac{\partial \phi(x)}{\partial x}\right| \tag{3}$$

$\det(J_\phi(\mathbf{x})) > 1$: Local expansion

Table 1. Registration quality assessment using Jacobian determinants

Segmentation Method	Registration Method	Mean Jacobian (LA)	% Neg. (LA)	Mean Jacobian (Scar)	% Neg. (Scar)
nnUNet	SimpleITK-DDVF	1.01	0.00	1.20	0.00
	ANTs (SyN)	0.97	0.16	0.99	0.03
	BSpline (FFD)	0.98	0.03	1.01	0.02
nnFormer	SimpleITK-DDVF	1.17	0.00	1.14	0.00
	ANTs (SyN)	0.98	0.20	1.11	0.00
	BSpline (FFD)	0.99	0.04	1.00	0.00

$\det(J_\phi(\mathbf{x})) < 1$: Local contraction

$\det(J_\phi(\mathbf{x})) = 0$: Non-physical folding (undesirable)

where ϕ is the deformation field and x is the spatial location (voxel co-ordinate). The Jacobian determinant at each voxel quantifies local volumetric changes induced by the registration transform. A physically plausible deformation is expected to have a mean Jacobian value close to 1 and a low percentage of negative Jacobian values, which typically indicates error in the registration process.

In Table 1 among the three methods, SimpleITK-DDVF produced the most stable deformation for both segmentation methods, with a mean Jacobian of 1.01 and 1.17 in the LA and 0% negative values, indicating smooth, volume-preserving warps. In the scar region, it yielded a higher mean Jacobian of 1.20 and 1.14, suggesting expansion potentially associated with pathological motion, with no folding observed.

ANTs (SyN) achieved a mean Jacobian of 0.97 and 0.98 in the LA, but the 0.16% and 0.20% negative values point to some instability in the deformation field. In the scar region, ANTs had the lowest mean Jacobian (0.99, 0.98) and a small percentage (0.03%, 0.0%) of negative values both for nnUNet and nnFormer, indicating slight compression near complex anatomical boundaries. Since ANTs is an intensity-based registration method, we utilized the segmented mask for registration. We then employed the Syn transformation and K nearest neighbor to ensure proper registration.

BSpline (FFD) showed a mean Jacobian of 0.98 and 0.99 in the LA cavity with only 0.03% and 0.04% negative values, and a scar region mean Jacobian of 1.01 with 0.02% folding, suggesting good anatomical alignment and regularity.

Table 2 summarizes motion-derived abnormal atrial wall coverage and scar detection outcomes across five patients using three deformable registration methods. For each method, the percentage of atrial wall exhibiting statistically abnormal motion (Abn. LA%) near atrial wall, motion-derived abnormal atrial wall volume (AMV) exceeding the Mahalanobis threshold, and abnormal motion–based scar detection (Detected) are reported. The abnormal motion volumes are expected to exceed LGE-defined scar cores, as motion abnormalities capture peri-scar and diffuse atrial remodeling that are mechanically impaired but not visible or consistently annotated on LGE-MRI. We notice that SimpleITK-based registration produces smoother, yet more localized deformation fields with higher contrast in stiff regions, enabling more consistent identification of statistically significant motion abnormalities compared to ANTs and BSpline methods. SimpleITK-DDVF consistently identifies abnormal

Table 2. Motion-derived abnormal atrial wall coverage and scar detection using Mahalanobis distance across 5 patients and 3 registration methods

Method	Patient	SimpleITK			ANTs			BSpline		
		Abn. LA (%)	AMV	Detected	Abn. LA (%)	AMV	Detected	Abn. LA (%)	AMV	Detected
nnUNet	Pat 01	73.9	62582.0	✓	2.7	27383.0	×	8.6	74901.0	×
	Pat 02	64.8	44512.1	✓	19.2	26543.0	✓	18.0	69037.0	✓
	Pat 03	71.9	48494.1	✓	3.0	35844.0	×	6.0	66457.0	×
	Pat 04	64.9	57499.5	✓	16.7	39773.0	✓	98.8	38092.0	✓
	Pat 05	73.8	52318.3	✓	13.7	34078.0	✓	55.5	57265.0	✓
nnFormer	Pat 01	59.7	44831.6	✓	0.7	27602.0	×	79.2	37518.0	✓
	Pat 02	58.6	55328.0	✓	11.5	41713.0	✓	97.4	39956.0	✓
	Pat 03	58.6	55830.9	✓	7.4	26762.0	×	85.6	28152.0	✓
	Pat 04	46.8	42423.5	✓	26.5	31809.0	✓	77.0	31862.0	✓
	Pat 05	56.7	48781.1	✓	17.2	33818.0	✓	78.5	38543.0	✓

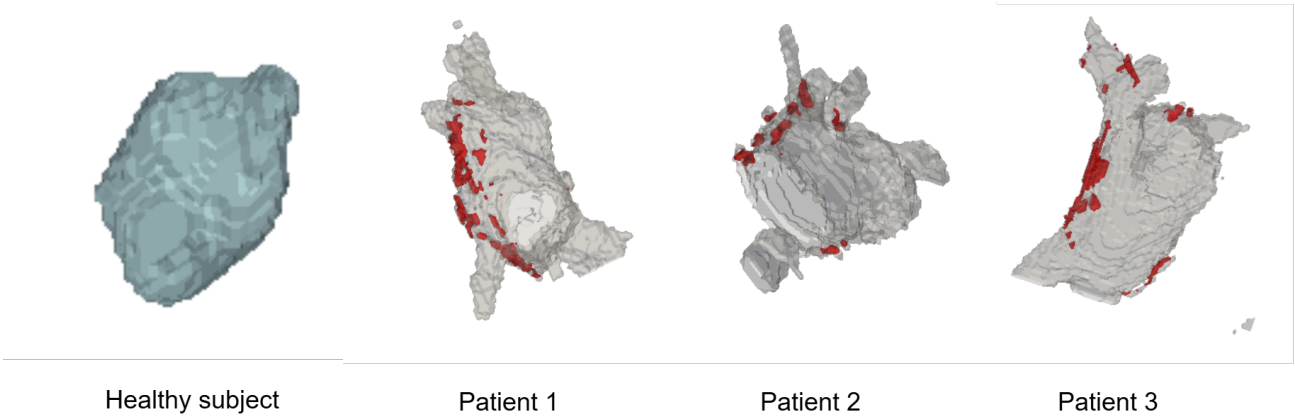

Figure 2. Visualization of abnormal motion regions identified using the Mahalanobis distance, shown in red, on 3D LA meshes from a healthy subject and a scarred patient following deformable registration.

motion across all patients, yielding high abnormal wall coverage and successful scar detection in every case. ANTs (SyN) and BSpline (FFD) show more variable performance, with only few failed attempts at detecting scar, despite substantial abnormal wall movement. Successful detection of the scar depends on the Mahalanobis threshold rather than the overall extent of abnormal motion alone, indicating significant deviation from healthy motion patterns. This behavior highlights that the proposed framework is prioritizing statistically significant and spatially coherent biomechanical abnormalities over global deformation magnitude, thereby reducing false-positive detections.

While the Mahalanobis distance approach detect motion abnormalities rather than scar precisely, the presence of scar is assessed based on whether regions in the deformation field exhibit Mahalanobis distances exceeding an adaptive threshold ($\mu + k\sigma$), indicating significant deviation from healthy motion patterns.

In Fig.2, we present a visualization of a 3D mesh of the LA from a healthy subject in the atlas and three scarred patients after deformable registration using simpleITK. The healthy atlas mesh demonstrates smooth and consistent morphology, representing typical LA motion patterns. In contrast, the warped LA cavity mesh of the scarred patient exhibits visible surface irregularities and abnormal deformation patterns associated with fibrotic tissue. These visual differences further support the effectiveness of our method in detecting abnormal mechanical behavior.

4. CONCLUSIONS

We introduced a motion based framework for LA scar detection and localization in Afib patients using static LGE-MRI and a healthy motion atlas. The identification of tissue regions that feature large Mahalanobis distances are desirable for ablation planning. By applying deformable registration and analyzing deviations in motion via Mahalanobis distance, our method enables scar detection and localization without the need for cine MRI, dynamic sequences, or highly accurate scar segmentation. Our pipeline also integrates two strong segmentation models to leverage the reliability of LA segmentation to ensure stable global alignment.

While scar segmentation is included only to provide anatomical context and patient-level confirmation, scar detection in our framework is fundamentally motion-driven and remains robust to segmentation inaccuracies. Our method identifies biomechanical abnormalities derived from motion deviation, and we use this information to inform ablation planning by recognizing regions of low viability or non-viable tissue. The key advantage of our pipeline lies in its validation on five patients. Our method detected scar regions using motion deviations despite a lower scar segmentation Dice score, proving that functional biomarkers surpass anatomical segmentation for pathology identification or are poorly visible by analyzing deviations in motion relative to a healthy atlas. The SimpleITK based registration demonstrated stable deformation fields and reliable motion-based scar detection across all test cases, supporting its use in future clinical integration.

5. ACKNOWLEDGEMENTS

We would like to acknowledge the generous support for this work by the the National Science Foundation - Division of Chemical, Bioengineering and Transport Systems under Award No. 2245152 and the National Institutes of Health – National Institute of General Medical Sciences under Award No. R35GM128877. We also acknowledge the use of ChatGPT[19] for minor assistance with code debugging and clean-up, as well as improving language clarity. Lastly, we acknowledge the computational support and access to the computing infrastructure provided by RIT's Research Computing Division.

REFERENCES

[1] Galazis, C., Bharath, A. A., and Varela, M., "High-resolution 3D maps of Left Atrial Displacements using an Unsupervised Image Registration Neural Network," *arXiv preprint arXiv:2309.02179* (2023).

[2] Tobon-Gomez, C., Geers, A. J., Peters, J., Weese, J., Pinto, K., Karim, R., Ammar, M., Daoudi, A., Margeta, J., Sandoval, Z., et al., "Benchmark for algorithms segmenting the left atrium from 3D CT and MRI datasets," *IEEE transactions on medical imaging* **34**(7), 1460–1473 (2015).

[3] Kundu, B., Khanal, B., Simon, R., and Linte, C. A., "Investigating the Domain Adaptability of General-Purpose Foundation Models for Left Atrium Segmentation from MR Images," in [*International Conference on Functional Imaging and Modeling of the Heart*], 275–287, Springer (2025).

[4] Punithakumar, K. and Noga, M., "Automated segmentation of the left atrium and scar using deep convolutional neural networks," in [*Challenge on Left Atrial and Scar Quantification and Segmentation*], 145–152, Springer (2022).

[5] Arega, T. W., Bricq, S., and Meriaudeau, F., "Using polynomial loss and uncertainty information for robust left atrial and scar quantification and segmentation," in [*Challenge on Left Atrial and Scar Quantification and Segmentation*], 133–144, Springer (2022).

[6] Zhang, Y., Meng, Y., and Zheng, Y., "Automatically segment the left atrium and scars from LGE-MRIs using a boundary-focused nnU-Net," in [*Challenge on Left Atrial and Scar Quantification and Segmentation*], 49–59, Springer (2022).

[7] Marrouche, N. F., Wilber, D., Hindricks, G., Jais, P., Akoum, N., Marchlinski, F., Kholmovski, E., Burgon, N., Hu, N., Mont, L., et al., "Association of atrial tissue fibrosis identified by delayed enhancement MRI and atrial fibrillation catheter ablation: the DECAAF study," *Jama* **311**(5), 498–506 (2014).

[8] Clinic, C., "Atrial fibrillation." 2022, https://my.clevelandclinic.org/health/diseases/16765-atrial-fibrillation-afib. (Accessed: 29 July 2024).

[9] Li, L., Zimmer, V. A., Schnabel, J. A., and Zhuang, X., "Medical image analysis on left atrial LGE MRI for atrial fibrillation studies: A review," *Medical image analysis* **77**, 102360 (2022).

[10] Li, L., Zimmer, V. A., Schnabel, J. A., and Zhuang, X., "AtrialGeneral: domain generalization for left atrial segmentation of multi-center LGE MRIs," in [*International Conference on Medical Image Computing and Computer-Assisted Intervention*], 557–566, Springer (2021).

[11] Galazis, C., Shepperd, S., Brouwer, E., Queirós, S., Alskaf, E., Anjari, M., Chiribiri, A., Lee, J., Bharath, A., and Varela, M., "Aladdin: High-Resolution Maps of Left Atrial Displacements and Strains Estimated with 3D ," (Sept. 2024).

[12] Isensee, F., Jaeger, P. F., Kohl, S. A., Petersen, J., and Maier-Hein, K. H., "nnU-Net: a self-configuring method for deep learning-based biomedical image segmentation," *Nature methods* **18**(2), 203–211 (2021).

[13] Zhou, H.-Y., Guo, J., Zhang, Y., Han, X., Yu, L., Wang, L., and Yu, Y., "nnformer: Volumetric medical image segmentation via a 3d transformer," *IEEE transactions on image processing* **32**, 4036–4045 (2023).

[14] Ericsson, A., Aljabar, P., and Rueckert, D., "Construction of a patient-specific atlas of the brain: Application to normal aging," in [*2008 5th IEEE international symposium on biomedical imaging: from nano to macro*], 480–483, IEEE (2008).

[15] Finnis, K., Starreveld, Y. P., Parrent, A., and Peters, T. M., "Subcortical physiology deformed into a patient-specific brain atlas for image-guided stereotaxy," in [*Medical Imaging 2002: Visualization, Image-Guided Procedures, and Display*], **4681**, 184–195, SPIE (2002).

[16] Daryanani, A., Dangi, S., Ben-Zikri, Y. K., and Linte, C. A., "A comparison study of atlas-based 3D cardiac MRI segmentation: global versus global and local transformations," in [*Medical Imaging 2016: Image-Guided Procedures, Robotic Interventions, and Modeling*], **9786**, 634–645, SPIE (2016).

[17] Frangi, A. F., Niessen, W. J., Rueckert, D., and Schnabel, J. A., "Automatic 3D ASM construction via atlas-based landmarking and volumetric elastic registration," in [*Biennial International Conference on Information Processing in Medical Imaging*], 78–91, Springer (2001).

[18] Galazis, C., Shepperd, S., Brouwer, E. J., Queirós, S., Alskaf, E., Anjari, M., Chiribiri, A., Lee, J., Bharath, A. A., and Varela, M., "High-resolution maps of left atrial displacements and strains estimated with 3D cine MRI using online learning neural networks," *IEEE transactions on medical imaging* (2025).

[19] OpenAI, "Chatgpt." https://chat.openai.com (2024). Large language model accessed January 2026.